

Flexible Linker-Based Triazine-Functionalized 2D Covalent Organic Frameworks for Supercapacitor and Gas Sorption Applications

Yogesh Kumar,[§] Ikrar Ahmad,[§] Anuj Rawat, Rakesh K. Pandey, Paritosh Mohanty, and Ravindra Pandey*



Cite This: *ACS Appl. Mater. Interfaces* 2024, 16, 11605–11616



Read Online

ACCESS |

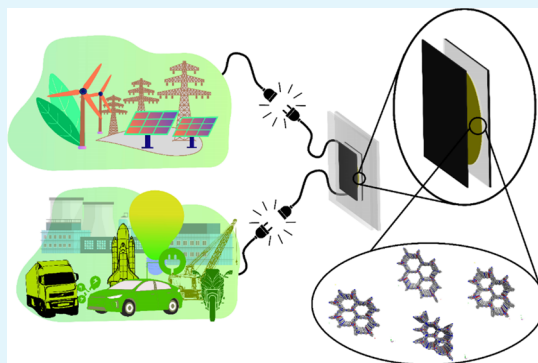
Metrics & More

Article Recommendations

Supporting Information

ABSTRACT: Covalent organic frameworks (COFs) having a large surface area, porosity, and substantial amounts of heteroatom content are recognized as the ideal class of materials for energy storage and gas sorption applications. In this work, we have synthesized four different porous COF materials by the polycondensation of a heteroatom-rich flexible triazine-based trialdehyde linker, namely 2,4,6-tris(4-formylphenoxy)-1,3,5-triazine (TPT-CHO), with four different triamine linkers. Triamine linkers were chosen based on differences in size, symmetry, planarity, and heteroatom content, leading to the synthesis of four different COF materials named IITR-COF-1, IITR-COF-2, IITR-COF-3, and IITR-COF-4. IITR-COF-1, synthesized within 24 h from the most planar and largest amine monomer, exhibited the largest Brunauer–Emmett–Teller (BET) surface area of $2830 \text{ m}^2 \text{ g}^{-1}$, superior crystallinity, and remarkable reproducibility compared to the other COFs. All of the synthesized COFs were explored for energy and gas storage applications. It is shown that the surface area and redox-active triazene rings in the materials have a profound effect on energy and gas storage enhancement. In a three-electrode setup, IITR-COF-1 achieved an electrochemical stability potential window (ESPW) of 2.0 V, demonstrating a high specific capacitance of 182.6 F g^{-1} with energy and power densities of 101.5 Wh kg^{-1} and 298.3 W kg^{-1} , respectively, at a current density of 0.3 A g^{-1} in $0.5 \text{ M K}_2\text{SO}_4$ (aq) with long-term durability. The symmetric supercapacitor of IITR-COF-1//IITR-COF-1 exhibited a notable specific capacitance of 30.5 F g^{-1} and an energy density of 17.0 Wh kg^{-1} at a current density of 0.12 A g^{-1} . At the same time, it demonstrated 111.3% retention of its initial specific capacitance after 10k charge–discharge cycles. Moreover, it exhibited exceptional CO_2 capture capacity of 25.90 and 10.10 wt % at 273 and 298 K, respectively, with 2.1 wt % of H_2 storage capacity at 77 K and 1 bar.

KEYWORDS: triazine functionalized, flexible linker, 2D hexagonal covalent organic frameworks, aqueous electrolyte, supercapacitors, gas adsorption



1. INTRODUCTION

Globalization and humanity's dependence on conventional fossil fuels have given rise to two critical challenges: the depletion of fossil fuel reservoirs and the increase of global warming. At present, fossil fuels account for more than 79% of the world's energy consumption. Nevertheless, projections from the World Energy Forum indicate that the Earth's reserves of gas, coal, and oil are anticipated to be depleted in under a century.¹ The combustion of these fuels releases harmful gases with carbon dioxide as a main contributor that plays a predominant role in various environmental issues, including the onset of climate change.² Two main solutions have been proposed to tackle these issues: decreasing dependence on fossil fuels by increasing clean energy usage and reducing CO_2 emissions from industrial sources. Recently, a rise in the adoption of clean energy sources such as wind and solar energy and the use of hydrogen as a clean fuel have been observed. Additionally, CO_2 capture from coal-fired power plants has begun using absorption to mitigate CO_2 -related pollution.³

However, these practices have some drawbacks. For instance, the variable nature of wind and solar power generation poses storage challenges due to the low power density of conventional batteries,⁴ and storing hydrogen as a fuel requires expensive multistage compression facilities.^{5,6} Conventional CO_2 absorption methods also require high energy for recovering the amine solutions.^{7,8} Therefore, it is crucial to address energy storage concerns for stabilizing power reserves, discover better methods for hydrogen storage as a fuel, and improve the capture of CO_2 to combat global warming.

For storing and utilizing energy efficiently, supercapacitors are becoming increasingly popular due to their affordability,

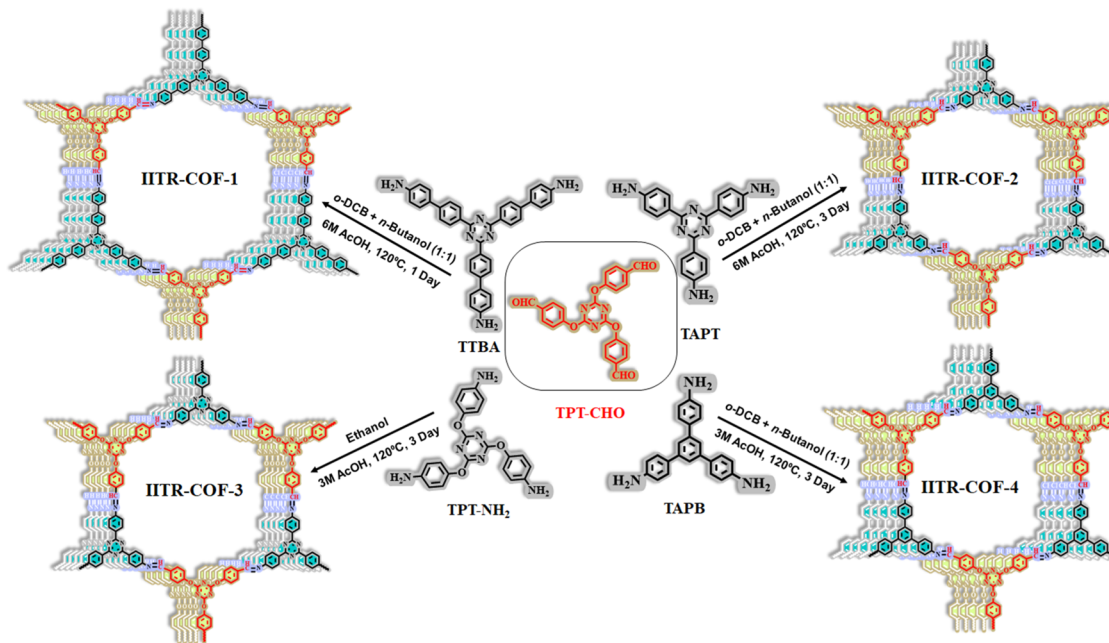
Received: January 3, 2024

Revised: February 12, 2024

Accepted: February 12, 2024

Published: February 26, 2024



Scheme 1. Schematic Strategy for the Synthesis of IITR-COFs from TPT-CHO with Four Different Amine Monomers

lightweight, high power delivery, rapid operation, and long cyclic stability. They find applications in heavy lifting with hybrid/electric cranes and fast electric cars.^{9–13} However, the performance of supercapacitors is reliant on the electrode material available, which must have a high surface area and porous network to facilitate electrolyte ion flow.¹⁴ Apart from that to solve the problem of hydrogen storage and CO₂ capture, adsorption technology utilizing porous materials is considered an effective, low-cost, and reliable alternative due to its simplicity, ease of operation, and high efficiency.^{15–19} Therefore, porous materials can play a crucial role in storing energy and hydrogen as well as capturing CO₂. Among various porous materials, covalent organic frameworks (COFs) are unique and have attracted significant attention due to their exceptional ability to precisely assemble organic building blocks at the molecular level, opening up vast possibilities for design.^{20–28} COFs are a perfect candidate for energy storage^{29–33} and CO₂ capture,^{34,35} owing to their remarkable porosity, tunable pore topologies, and unique pore shapes, making them a promising next-generation solid adsorbent with immense applications in various fields.^{36–41} To make COFs effective in energy and gas storage applications, a combination of a large surface area, an active redox site, and extended electronic conjugation is necessary. Both theoretical and experimental studies have indicated that the presence of heteroatoms, such as N, O, B, S, and P in polymeric or carbonaceous materials, has shown promising performance for charge storage processes. This is attributed to the coupling of delocalized lone pairs of heteroatoms with the electrons present in the framework, providing the necessary transport of electrons.^{42–45} Therefore, basic functionalities such as imine ($-C=N$), triazine or azo ($-N=N$) have gained special interest due to their redox activity^{46,47} and CO₂-philic character in building COFs for energy storage as well as CO₂ capture.^{48–51}

In this study, we have selected a heteroatom-rich flexible triazine-based trialdehyde linker 2,4,6-tris(4-formylphenoxy)-1,3,5-triazine (TPT-CHO) as the main building block to synthesize four different COFs. Different COFs have been

synthesized by changing the amine linker such as IITR-COF-1 by using 4',4'',4'''-(1,3,5-triazine-2,4,6-triyl)tris([1,1'-biphenyl]-4-amine)) (TTBA), IITR-COF-2 by using 2,4,6-tris(4-aminophenyl)-1,3,5-triazine (TAPT), IITR-COF-3 by using 2,4,6-tris(4-aminophenoxy)-1,3,5-triazine (TPT-NH₂), and IITR-COF-4 by using 1,3,5-tris(4'-aminophenyl)benzene (TAPB). In the present work, the effects of the planarity, size, symmetry, and heteroatom content of the monomers on the energy and gas storage properties have been carried out (Scheme 1).

2. EXPERIMENTAL SECTION

2.1. Chemicals and Materials. 2,4,6-Tris(4-formylphenoxy)-1,3,5-triazine (TPT-CHO); 4',4'',4'''-(1,3,5-Triazine-2,4,6-triyl)tris(([1,1'-biphenyl]-4-amine)) (TTBA); 2,4,6-tris(4-aminophenyl)-1,3,5-triazine (TAPT); and 2,4,6-tris(4-aminophenoxy)-1,3,5-triazine (TPT-NH₂) were purchased from Indus-bio chem, and 1,3,5-tris(4'-aminophenyl)benzene (TAPB) was purchased from TCI. Solvents, such as 1,2-dichlorobenzene (*o*-DCB), *n*-butanol, mesitylene, dioxane, and acetic acid, were procured from SRL. All chemicals utilized were of analytical grade and were employed without further purification. In all of the experiments, freshly prepared deionized water (having a conductivity of 18.2 MΩ) from Millipore was used.

2.2. Instrumentation. Powder X-ray diffraction (PXRD) patterns were recorded using a Rigaku, MicroMax-007HF, using a high-intensity microfocus rotating anode X-ray generator and Cu K α ($\lambda = 1.54 \text{ \AA}$) radiation source with a Ni filter. Fourier-transform infrared (FT-IR) spectra were measured in the wavenumber range of 4000–500 cm⁻¹ with a background correction using an FT-IR spectrophotometer manufactured by Bruker. The thermogravimetric analysis (TGA) of the samples was conducted by utilizing an EXSTAR TG/DTA6300 TGA instrument. Field emission scanning electron microscopy (FE-SEM) images and energy-dispersive X-ray (EDX) analysis were performed using Apreo S Low Vac purchased by Thermo Fisher. Transmission electron micrograph (TEM) analysis and selected area electron diffraction (SAED) measurements were obtained on an FEI TECHNAI G2 20 S-TWIN at an operating voltage of 200 kV equipped with a charged-coupled device (CCD) camera. Samples were prepared by sonicating a small quantity of solid sample in methanol for approximately 15–20 min. Subsequently, a droplet of this solution was carefully dropped onto a carbon-coated copper grid (G200, size

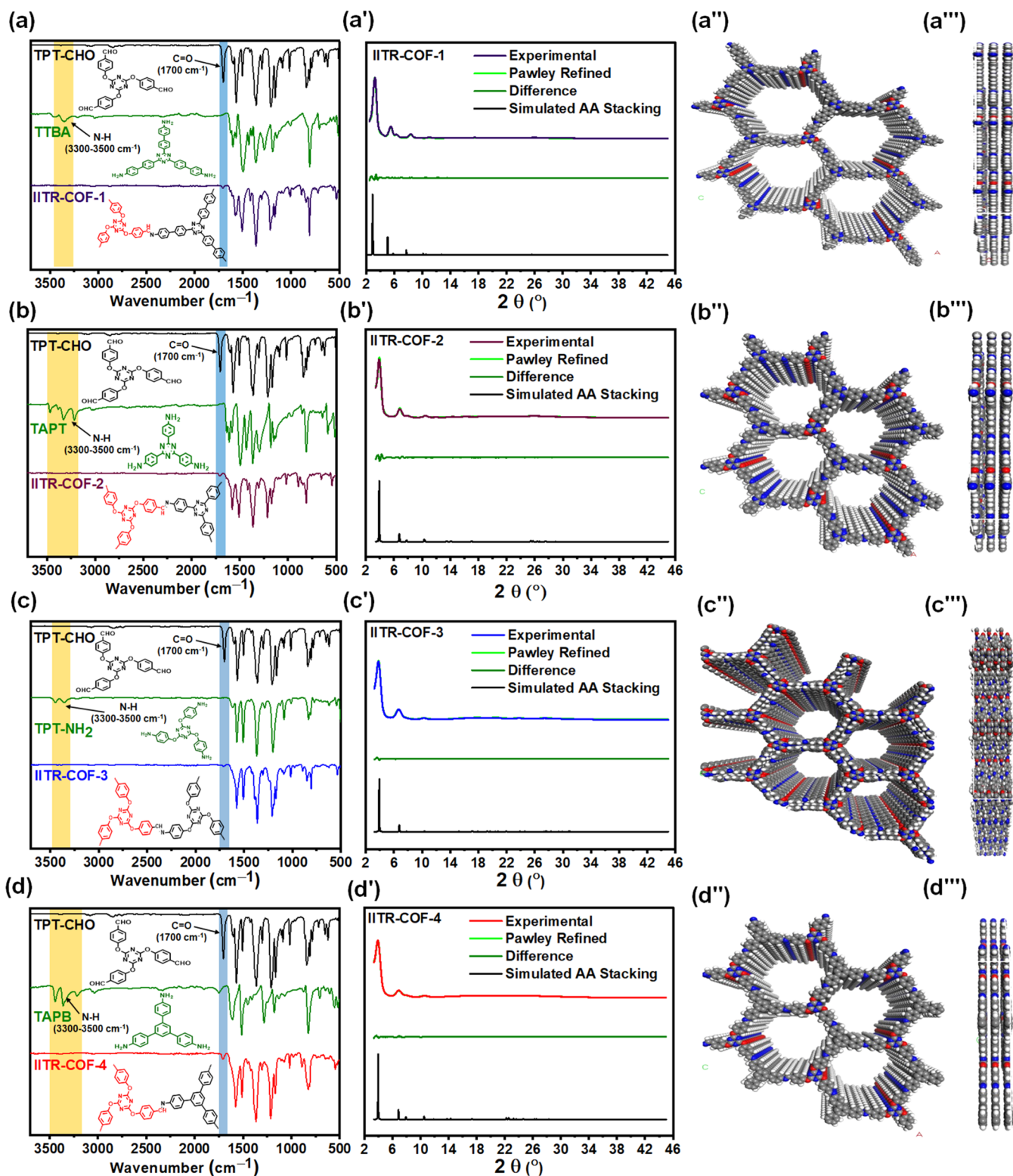


Figure 1. FT-IR spectra of (a) IIITR-COF-1, (b) IIITR-COF-2, (c) IIITR-COF-3, and (d) IIITR-COF-4. (a') Experimental PXRD patterns of (a') IIITR-COF-1, (b') IIITR-COF-2, (c') IIITR-COF-3, and (d') IIITR-COF-4. These results are compared with the simulated patterns (black) calculated for the Pawley refinement (green). (a''–d'') Top view and (a–d) side view of space-filling models of the IIITR-COFs.

3.05 mm). X-ray photoelectron spectroscopy (XPS) measurements were carried out using a PHI 5000 Versa Probe III (supplied by ULVAC-PHI Inc., Japan). All electrochemical measurements, including cyclic voltammetry (CV), galvanostatic charge/discharge (GCD), linear sweep voltammetry (LSV), and electrochemical impedance spectroscopy (EIS), were conducted by using a Metrohm Autolab M-

204 electrochemical workstation equipped with NOVA 2.0 software. Gas sorption experiments were carried out using Autosorb-iQ2 (Quantachrome Instruments). The N₂ sorption analyses were performed at 77 K and 1 bar. The CO₂ sorption analyses were carried out at 0 and 25 °C. The H₂ storage capacity was measured at 77 K and 1 bar.

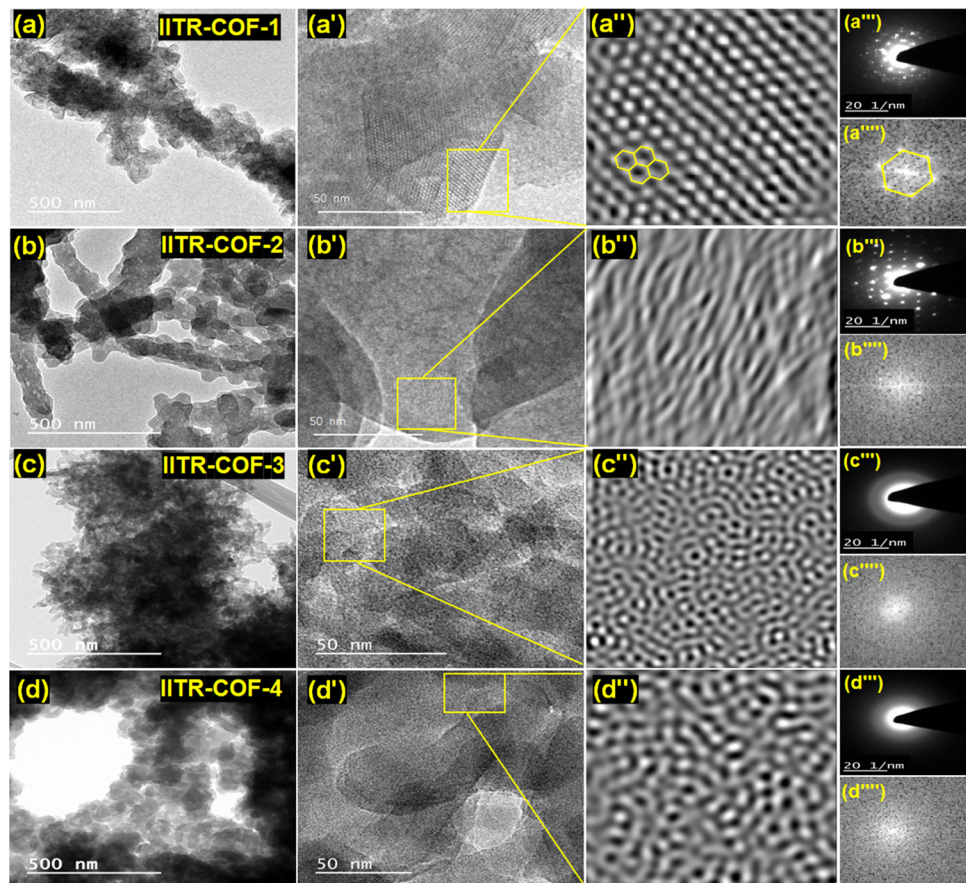


Figure 2. (a–d) TEM images of IITR-COF-1, IITR-COF-2, IITR-COF-3, and IITR-COF-4; (a'–d') and their corresponding lattice fringes; (a''–d'') the zoomed portion of the yellow square showing the lattice fringes; (a'''–d''') their corresponding high SAED pattern; and (a'''–d''') FFT, respectively.

2.3. Synthesis of Covalent Organic Frameworks. **2.3.1. Synthesis of IITR-COF-1.** TPT-CHO (44.1 mg, 0.1 mmol) and TTBA (58.2 mg, 0.1 mmol) were added in a 10 mL Schlenk tube; after that, the monomers were dissolved in 2 mL of solvent mixture of *o*-DCB and *n*-butanol (1:1). Then, 0.2 mL of 6 M acetic acid is added as a catalyst, and the mixture was degassed using three freeze–pump–thaw cycles. After that, the mixture was heated at 120 °C in a silicon oil bath for 24 h. The obtained yellow precipitates were washed several times with methanol and acetone. The COF powder was finally dried at 100 °C in an oven for 12 h, resulting in a yield of 86.4 mg (89%).

2.3.2. Synthesis of IITR-COF-2. For the synthesis of IITR-COF-2, TPT-CHO (17.7 mg, 0.05 mmol) and TAPT (22.0 mg, 0.05 mmol) were dissolved in 1 mL of a solvent mixture of *o*-DCB and *n*-butanol (1:1), along with 0.1 mL of 6 M acetic acid. The resulting mixture underwent heating in a silicon oil bath at 120 °C for a duration of 72 h followed by three freeze–pump–thaw cycles. Subsequently, the isolated product was subjected to filtration and washed alternately with acetone and THF. Following this, the product was dried in an oven for 12 h at 100 °C. The yield of the final product obtained was 33.1 mg (89%).

2.3.3. Synthesis of IITR-COF-3. The synthesis of IITR-COF-3 was accomplished by combining 44.1 mg (0.1 mmol) of TPT-CHO with 40.2 mg (0.1 mmol) of TPT-NH₂ in a Schlenk tube containing 2.4 mL of ethanol as the solvent. After that, the mixture was sonicated for 5 min, and then, 0.48 mL of 3 M acetic acid was added. Subsequently, the reaction mixture underwent degassing through three freeze–pump–thaw cycles. The mixture was then heated at 120 °C for 72 h, and the resulting product was filtered, washed with acetone, and dried in an oven at 100 °C for 12 h. The yield of the obtained final COF powder was 69.3 mg (88%).

2.3.4. Synthesis of IITR-COF-4. The procedure resembles previous ones, but in this instance, TAPB (35.1 mg, 0.1 mmol) was mixed with TPT-CHO (44.1 mg, 0.1 mmol) in 2 mL of a solvent mixture of *o*-DCB and *n*-butanol (1:1). After that, the mixture was sonicated for 5 min, and then, 0.4 mL of 3 M acetic acid was added. Then, the mixture was heated for 72 h followed by degassing at 77 K. The isolated product was filtered and washed with acetone and dried in an oven for 12 h at 100 °C. The yield of the obtained COF is 62 mg (84%).

2.4. Fabrication of Electrodes. For the fabrication of electrodes, a homogeneous slurry of COF samples was prepared by mixing the 40 mg of synthesized COF powder, 5 mg of poly(vinylidene difluoride) (PVDF) binder, and 5 mg of activated carbon (8:1:1) in 1 mL of *N*-methyl-2-pyrrolidone (NMP) solvent. For a three-electrode setup, the COF slurry (~1 mg cm⁻²) was applied onto 0.2 mm graphite sheet (1 cm × 1 cm) as a working electrode. The reference electrode was Ag/AgCl (3 M KCl), and a platinum wire served as the counter electrode. The working electrode was dried overnight in a vacuum oven at 60 °C. For the symmetrical supercapacitor cell (SSC), electrodes were fabricated on a 0.5 mm graphite sheet (1 cm × 1.5 cm) for both positive and negative electrodes, separated by Whatman filter paper, while the total active mass loading on both electrodes was ~2.5 mg. During the experiments, 50 CV cycles were conducted in both three-electrode and symmetric cell setups to achieve stability before recording data.

3. RESULTS AND DISCUSSION

3.1. Characterization of the Synthesized COFs. In this study, we have synthesized a series of four flexible linker-based triazene-functionalized COFs using the polycondensation reaction. The success of the polycondensation reaction yielding

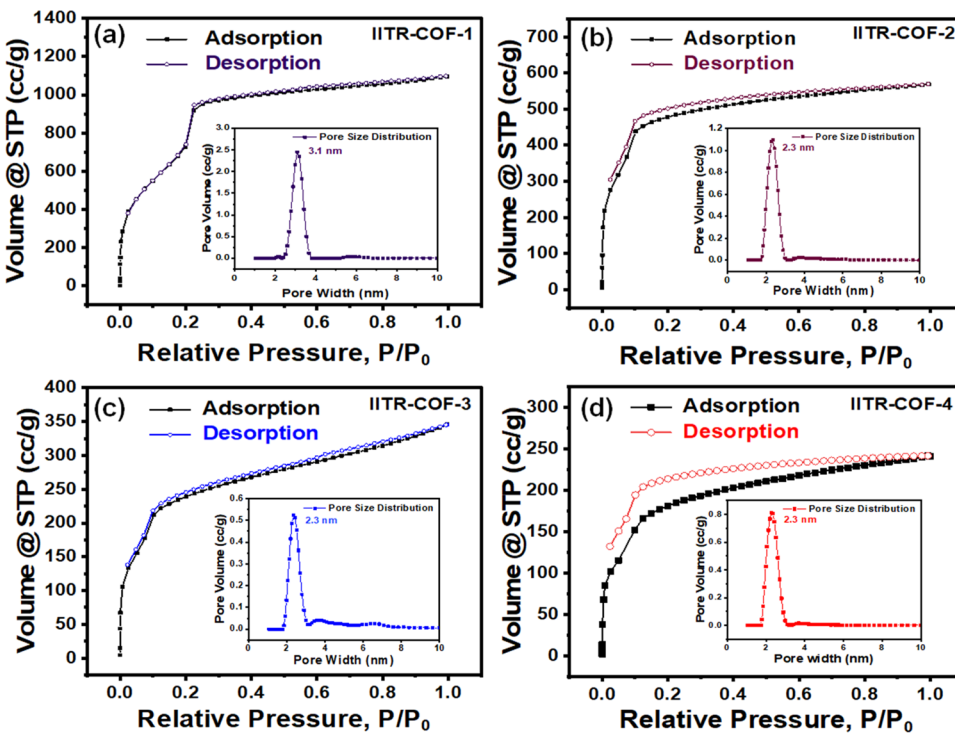


Figure 3. N_2 adsorption (filled rectangle) and desorption (empty circle) study of (a) IITR-COF-1, (b) IITR-COF-2, (c) IITR-COF-3, and (d) IITR-COF-4 and their respective pore size distributions (inset).

the COFs was confirmed by using Fourier-transform infrared (FT-IR) spectroscopy and X-ray photoelectron spectroscopy (XPS). The FT-IR spectra (Figure 1a–d) exhibited multiple peaks corresponding to the C=O group, aromatic C=C group, and the –NH₂ group. However, for the clear interpretation of FT-IR data more explicitly, we have focused only on the functionalized NH₂ and C=O groups. The amine monomers were identified by characteristic peaks at 3460–3207 cm⁻¹ for the NH₂ groups, whereas the aldehyde monomer was identified mainly by the peak at roughly 1702 cm⁻¹ for the C=O group. The FT-IR spectra of the IITR-COFs after polycondensation showed almost the disappearance of the peaks for the NH₂ and C=O units of the monomers and the appearance of a new signal at 1627–1616 cm⁻¹ representing the C=N stretching vibrations, which suggests the formation of the expected COFs via Schiff-base polycondensation reactions. Weak signals at 3475–3380 and 1703–1697 cm⁻¹ indicate the presence of the NH₂ and C=O groups at the terminal position of the resulting COFs, respectively. Furthermore, XPS demonstrated the formation of an imine linkage in IITR-COFs (Figure S1). The peaks of C 1s, N 1s, and O 1s appeared in the broad survey XPS spectrum. In high-resolution XPS, C 1s spectra, the three peaks observed for all of the COF materials at the binding energies of nearly 284.7 eV for C=C, 286.3 eV for (C=N)_{imine}, and 289.0 eV for (C=N)_{triazine}.⁵² The N 1s bands for each COF were deconvoluted into two peaks and were assigned to the nitrogen in the imine bond and triazine rings (Figure S1b', b'', b''', b'''''). The findings from both Fourier-transform infrared (FT-IR) and XPS analyses provided confirmation of the successful synthesis of IITR-COFs.

The crystal structure of the IITR-COFs was confirmed by using powder X-ray diffraction (PXRD) in combination with a simulated XRD pattern (Figure 1a'–d'). Moreover, the PXRD pattern of IITR-COF-1 synthesized on different time scales and

different solvent mixtures is shown in Figure S2. The sharp peaks in the PXRD patterns confirmed the formation of the crystalline covalent organic frameworks. The PXRD diffraction peaks of IITR-COF-1 were observed at 3.25°, with additional peaks at 5.52, 6.38, and 8.35°, which corresponded to the (100), (110), (200), and (210) facets, respectively (Figure 1a'). Similarly, IITR-COF-2 displayed a prominent peak at 4.10°, along with weaker peaks at 7.08, 8.12, and 10.75°, attributed to the (100), (110), (200), and (210) facets, respectively (Figure 1b'). Moving on to Figure 1c', the PXRD pattern of IITR-COF-3 exhibited a strong diffraction intensity at 3.90°, corresponding to the (100) plane, along with faint peaks at 6.76, 7.72, and 10.32°, representing the (110), (200), and (210) facets, respectively. Finally, Figure 1d' demonstrated that IITR-COF-4 displayed a strong peak at 3.93°, corresponding to the (100) plane, alongside weaker peaks at 6.75, 7.90, and 10.35°, indicating the (100), (110), (200), and (210) diffractions, respectively. The experimental XRD pattern of all COFs closely resembled the simulated pattern derived from the AA stacking by using the Material Studio software depicted in Figure 1. By performing Pawley refinement on the experimental PXRD data, we determined the unit cell characteristics for IITR-COF-1 to be $a = b = 35 \text{ \AA}$, $c = 3.35 \text{ \AA}$, and $\alpha = \beta = 90^\circ$, $\gamma = 120^\circ$. For IITR-COF-2, the unit cell parameters were found to be $a = b = 26.2 \text{ \AA}$, $c = 3.5 \text{ \AA}$, and $\alpha = 89.6^\circ$, $\beta = 90.2^\circ$, $\gamma = 120.6^\circ$. Likewise, the unit cell characteristics of IITR-COF-3 were identified as $a = b = 26.1 \text{ \AA}$, $c = 6.4 \text{ \AA}$, and $\alpha = 90^\circ$, $\beta = 90^\circ$, and $\gamma = 120^\circ$, and for IITR-COF-4, the obtained unit cell parameters were $a = b = 28.8 \text{ \AA}$ and $c = 4.4 \text{ \AA}$, and $\alpha = 90^\circ$, $\beta = 90^\circ$, and $\gamma = 120^\circ$. The PXRD data and structural analysis of IITR-COF-2, IITR-COF-3, and IITR-COF-4 were consistent with the earlier reports.^{53–56} The morphology of the synthesized COFs was visualized by transmission electron microscopy (TEM) and field emission scanning electron microscopy (FE-SEM). TEM images of the

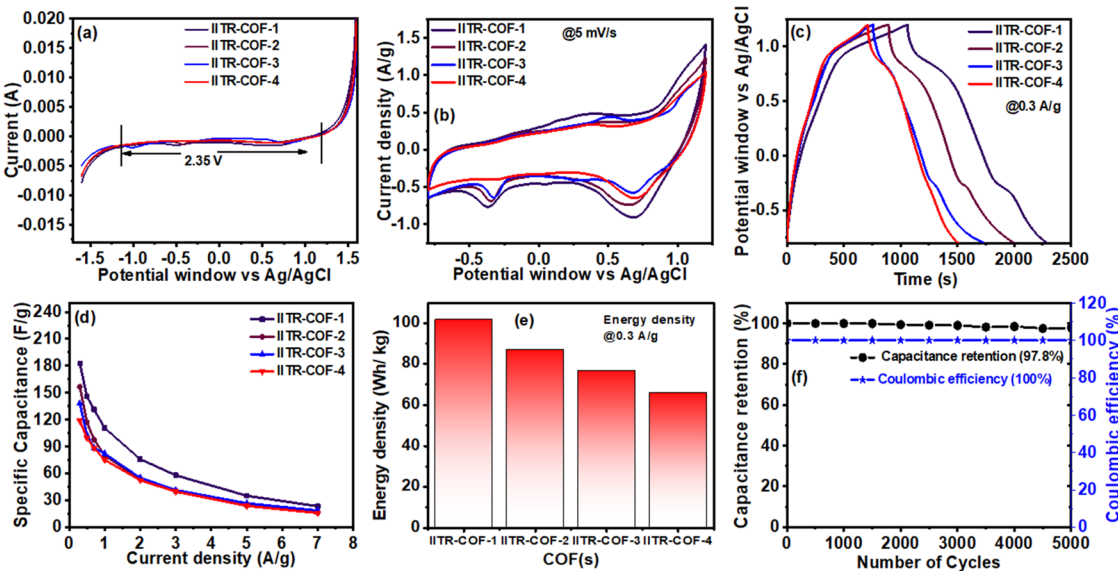


Figure 4. Electrochemical performances in a three-electrode setup: (a) LSV measurements of IITR-COF-1, IITR-COF-2, IITR-COF-3, and IITR-COF-4 in 0.5 M K_2SO_4 (aq) at 10 mV s^{-1} ; (b) CV and (c) GCD measurements in the 0.5 M K_2SO_4 (aq); (d) Ragone plot of all COFs at $0.3\text{--}7 \text{ A g}^{-1}$ current density; (e) bar plot of all COFs at 0.3 A g^{-1} ; and (f) cyclic stability and Coulombic efficiency at 3 A g^{-1} of IITR-COF-1.

IITR-COFs (Figure 2) showed crystalline domains and revealed the porous nature of COFs. Selected area electron diffraction (SAED) and fast Fourier transformation (FFT) patterns confirmed that among all four COFs, IITR-COF-1 and IITR-COF-2 are more crystalline in nature. Additionally, the transmission electron microscopy (TEM) image of IITR-COF-1 provided further evidence, confirming its superior porosity compared to that of other COFs. In FE-SEM analysis (Figure S3), IITR-COF-1 exhibited morphology of clustered spherical particles ranging from 0.1 to $0.5 \mu\text{m}$. Conversely, the particles of IITR-COF-2 formed agglomerated nanorods, while IITR-COF-3 displayed a morphology characterized by nanofibers, and particles of IITR-COF-4 were agglomerated in a spherical shape, with particle sizes ranging from 0.5 to $1.0 \mu\text{m}$. EDX analysis (Figure S3) also confirms the similar trend of heteroatom content in all COFs as calculated from XPS analysis.

Elemental mapping shows the homogeneous distribution of carbon, nitrogen, and oxygen in all of the COFs (Figure S3). Moreover, the thermogravimetric analysis of the IITR-COFs (Figure S4) indicated that all COFs, except for IITR-COF-3, exhibited thermal stability up to 400°C . On the other hand, IITR-COF-3 demonstrated thermal stability up to 375°C . This difference in thermal stability can be attributed to the high flexibility of the amine and aldehyde linker present in this COF.

3.2. Textural Properties of the COFs. The textural properties of all of the synthesized IITR-COFs were analyzed by an N_2 sorption isotherm measured at 77 K . All of the synthesized COFs show a type-IV isotherm (Figure 3) with a minor desorption hysteresis that suggests that all of the materials possess the majority of micropores with a smaller number of mesopores. Moreover, in all of the COFs, two knees were observed, and after the second knee, the curve became almost saturated, indicating the complete filling of all of the micropores by the N_2 molecules. The incomplete closing of the desorption branch is attributed to the swelling effect, which is generally observed in the COFs due to their flexible nature. The specific surface area calculated from the BET model (SA_{BET}) of all of the materials is as follows: IITR-COF-1 ($2830 \text{ m}^2 \text{ g}^{-1}$) > IITR-COF-2 ($1274 \text{ m}^2 \text{ g}^{-1}$) > IITR-COF-3 ($876 \text{ m}^2 \text{ g}^{-1}$) > IITR-

COF-4 ($660 \text{ m}^2 \text{ g}^{-1}$). Therefore, these data indicate that the three main factors that affect the BET surface area of the COFs are symmetry, planarity, and size of the monomers.

To examine the source of crystallinity, ease of synthesis, particularly for IITR-COF-1, and surface area patterns in the four COFs, the monomer geometries were optimized through density functional theory (DFT) calculations utilizing the B3LYP/6-31G(d,p) basis set (Table S1). The geometry optimization and torsional angle calculations revealed that TTBA and TAPT monomers exhibit a high degree of symmetry, rigidity, and planarity. However, TPT-CHO and TPT-NH₂ are highly flexible and unsymmetrical monomers. Geometry optimization of TAPB indicated the symmetric nature of the monomer, but the torsional angle (38°) suggested that it is not entirely planar due to the lack of a planar triazine ring.⁵⁷ Based on the DFT calculations of the monomers, it can be inferred that IITR-COF-1 and IITR-COF-2 exhibited superior symmetry. This characteristic contributes to their enhanced crystalline nature, as corroborated by TEM analysis. On the other hand, IITR-COF-3 and IITR-COF-4 are unsymmetrical COFs due to highly flexible TPT-NH₂ and nonplanar TAPB monomers, respectively. The ease of synthesis for IITR-COF-1 is attributed to the highly planar, symmetrical, rigid, and large-sized TTBA monomer, which can readily accommodate the highly flexible aldehyde linker (TPT-CHO), leading to the rapid formation of a crystalline framework. From this result, it can be concluded that not only the tautomerisation⁵⁸ but also the monomer's size and symmetry play a vital role in the synthesis of COF.⁵⁹ The highest SA_{BET} of IITR-COF-1 could also be attributed to high symmetry and the large size of the TTBA linker with additional phenyl groups, which can provide more surface areas to the final polymeric framework. The nonlocal density functional theory method has been used to calculate the pore size distributions of the COFs. A uniform pore size distribution of 3.09 nm for IITR-COF-1 and 2.35 nm for all other three COFs has been obtained. The total pore volume of the synthesized materials was estimated as 1.66 , 0.90 , 0.80 , and $0.53 \text{ cm}^3 \text{ g}^{-1}$ for IITR-COF-1, IITR-COF-2, IITR-COF-3, and IITR-COF-4, respectively.

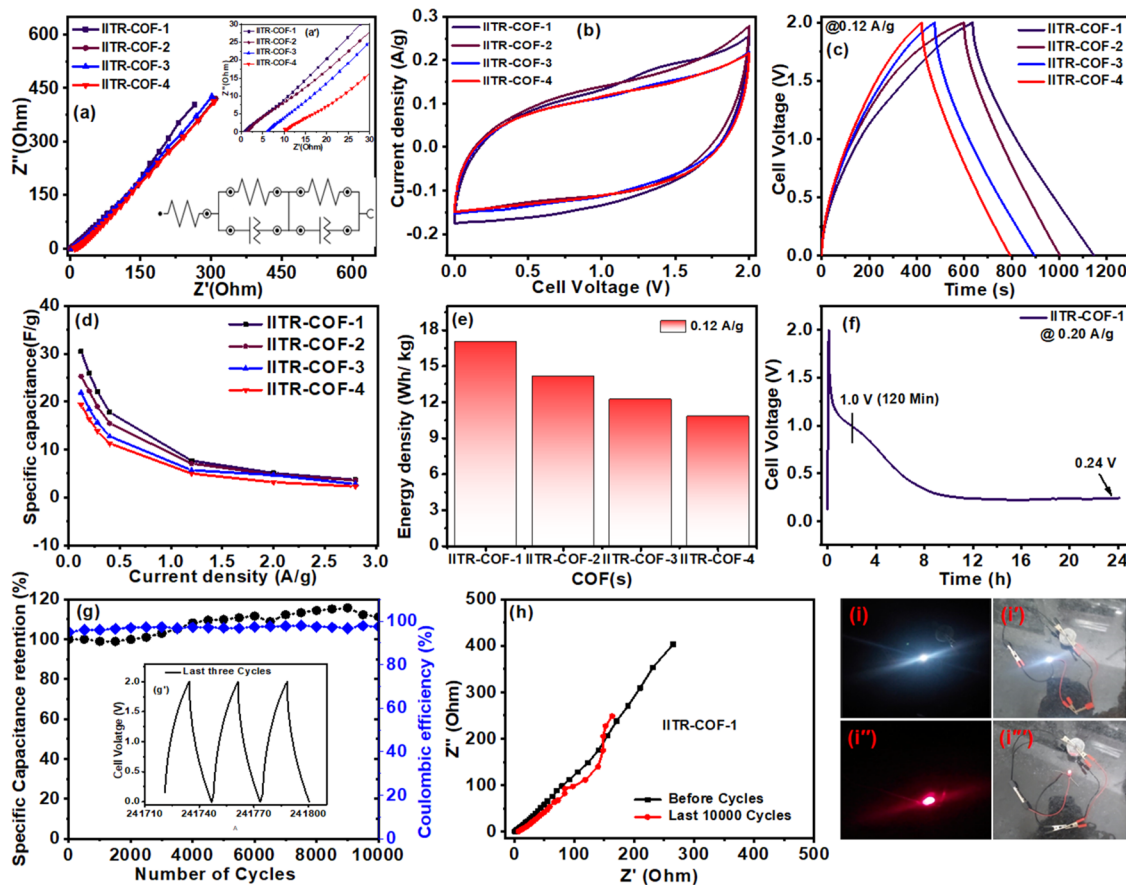


Figure 5. Electrochemical performances in a symmetric supercapacitor cell. (a) Nyquist plots demonstrating the changes in impedance of IITR-COF-1, IITR-COF-2, IITR-COF-3, and IITR-COF-4 in $0.5 \text{ M K}_2\text{SO}_4$ (aq), (a') extended impedance curves inset (inset); (b) CV and (c) GCD measurements in the $0.5 \text{ M K}_2\text{SO}_4$ (aq); (d) Ragone plot of all COFs; (e) bar plot of all COFs at 0.12 A g^{-1} ; (f) self-discharge curve at 0.2 A g^{-1} ; (g) cyclic stability and Coulombic efficiency at 1.2 A g^{-1} ; (h) EIS plot before and after 10,000 cycles, (i, i'') white LED illumination in the dark and light, and (i'', i''') red LED illumination in the dark and light.

3.3. Supercapacitor Application. To explore the potential of the synthesized materials in energy storage applications, we fabricated the electrodes of these materials on the graphite sheet, and cyclic voltammetric analysis was done in three- and two-electrode (symmetric supercapacitor) setup. The selection of an appropriate electrolyte is crucial for developing an efficient supercapacitor. The chosen electrolyte must exhibit electrochemical stability over a wide potential range, be inert, economically viable, environmentally friendly, and demonstrate high ionic conductivity.⁶⁰ Supercapacitor devices commonly employ organic and ionic liquid (IL) electrolytes to attain a high operational cell voltage. However, they face challenges of low ionic conductivity and high viscosity, limited power capabilities.⁶¹ To overcome these challenges, there has been a recent emphasis on investigating aqueous electrolytes because of their affordability, high ionic conductivity, nonflammability, and ease of cell fabrication.⁶² Neutral aqueous electrolytes like Li_2SO_4 , Na_2SO_4 , and K_2SO_4 have demonstrated the ability to expand the potential window of symmetric supercapacitors up to 2.2 V.⁶³

3.3.1. Three-Electrode Setup. The electrochemical stability of the potential window (ESPW) was determined for the fabricated electrodes of all of the COF materials. This investigation was carried out using linear sweep voltammetry (LSV) measurements in a $0.5 \text{ M K}_2\text{SO}_4$ (aq) solution (Figure 4a). In the $0.5 \text{ M K}_2\text{SO}_4$ (aq), the LSV curves clearly demonstrated the stable potential window of about 2 V (-0.8

to $+1.2$) for all COFs. The ESPW of the COFs was further examined by performing the cyclic voltammograms (CV) in the potential window range of -0.8 to 1.2 V. The experiments confirmed that the operational potential window is 2.0 V, with cathodic and anodic potential values of -0.8 and $+1.2$ V, respectively. Beyond this range, the hydrogen evolution reaction (HER) and oxygen evolution reaction (OER) become noticeable (Figure S5, panels a, c, e, and g). Interestingly, the appearance of pseudo peaks starts appearing at an anodic potential of ~ 0.35 V, suggesting that they possibly arise due to the oxidation of nascent hydrogen produced/trapped in porous structure at these sites (Figure S5). During the cathodic cycle, CV plots of IITR-COF-1, IITR-COF-2, and IITR-COF-3 reveal two distinct peaks around 0.68 and -0.36 V. These peaks suggest the potential involvement of pseudocapacitive reactions associated with the two redox-active triazine rings incorporated in the COF(s) matrix. Interestingly, in the case of IITR-COF-4, the peak at -0.36 V was not observed, possibly indicating the absence of a triazine ring in the amine linker. The specific capacitance of all COFs was examined by using galvanostatic charge–discharge (GCD) experiments at a range of current densities ($0.3, 0.5, 0.7, 1, 3, 5$, and 7 A g^{-1}) in the potential window range from -0.8 to 1.2 V (Figure S5, panels b, d, f, and h). The curves depicted in Figure 4c for all COFs exhibited an almost triangular shape. The specific capacitance (F g^{-1}) and areal capacitance (mF cm^{-2}) were determined at a current

density of 0.3 A g^{-1} , resulting in the values of 182.6, 156.5, 138.0, and 118.5, and 183.7, 165.2, 146.1, and 119.1 for IITR-COF-1 to IITR-COF-4, respectively (Figure 4d). The CV and GCD analyses suggest that the charge storage mechanism of these materials is notably influenced by the electric double-layer capacitance (EDLCs), underscoring the importance of their substantial surface area.⁶⁴ Furthermore, the inclusion of redox-active triazene rings and imine bonds in the structure enhances pseudocapacitance (PCs). The possible redox reactions of triazene units and imine bond are illustrated in Scheme S1, and a comparable mechanism has been documented in the existing previous literature as well.^{47,65,66} Interestingly, the redox activity persists even under high scan rates in both CV and GCD cycles, indicating substantial faradaic activity. Besides this, the materials exhibited impressive energy density (Wh kg^{-1})@power density (W kg^{-1}) of 101.5@298.3 for COF-1, 86.9@284.2 for COF-2, 76.7@283.4 for COF-3, and 65.8@298.3 for COF-4 (Figure 4e).

Among all COFs, IITR-COF-1 exhibited superior energy storage capabilities, due to the increased wettability, efficient electron transport, and participation of EDLCs in the energy storage process, and this is facilitated by its extensive π -electron conjugate system, high surface area, and uniform pores. Additionally, IITR-COF-1 exhibited excellent electrochemical stability, maintaining 97.8% of its initial specific capacitance and achieving 100% Coulombic efficiency at a current density of 3 A g^{-1} , even after 5000 charge–discharge cycles.

3.3.2. Symmetric Supercapacitor Cells (Two-Electrode Setup). Electrochemical impedance spectroscopy (EIS) analysis is widely used to investigate the mechanism of charge storage for supercapacitors. For this purpose, the EIS of the as-designed symmetric supercapacitor device of all four COFs was recorded. The electrode resistance (R_s , Ω) and charge transfer resistance (R_{ct} , Ω) of IITR-COF-1 to IITR-COF-4 were observed to be 0.86, 1.47, 6.00, and 10.07, and 0.31, 0.33, 0.42, and 0.53, respectively. The increases in electrode resistance and charge transfer resistance are in accordance with the surface area trend of COFs. This trend in electrode resistance and charge transfer resistance with the surface area facilitates the availability of more active sites for ion absorption and the rapid diffusion of electrolyte ions within the material. Besides that, the interconnected pores in the COFs create pathways for efficient electron transport, thereby reducing the risk of ion aggregation. Also, the high pore volume provides better availability of the electrolyte to the inside of the material. The real utility of as-fabricated electrode materials was explored by making a symmetrical supercapacitor cell (IITR-COF-1, IITR-COF-2, IITR-COF-3, and IITR-COF-4) in $0.5 \text{ M K}_2\text{SO}_4$ (aq). These performances were further examined by performing the cyclic voltammograms at scan rates ranging from 5 to 500 mV s^{-1} (Figures 5b and S6). The curves obtained at various scan rates exhibited a rectangular shape, indicating favorable capacitive behavior within the potential window of 2.0 V. Notably, IITR-COF-1 exhibited a small peak $\sim 1.4 \text{ V}$ at lower scan rates, likely due to its redox-active triazine ring and porous structure. The specific capacitance for these cells was measured by performing the galvanostatic charge–discharge (GCD) curves for the cell voltage of 2.0 V at different current densities from 0.12 to 2.8 A g^{-1} . The GCD curves of IITR-COF-1, IITR-COF-2, IITR-COF-3, and IITR-COF-4 were obtained nearly triangular shaped (Figures 5c and S6 panels b, d, f, h). From these curves, the specific capacitance (F g^{-1}) for the current density 0.12 A g^{-1} was calculated to be 30.5, 25.3, 21.9, and 19.4 (Figure 5d). The

designed symmetric supercapacitor devices exhibited impressive energy density (Wh kg^{-1})@power density (W kg^{-1}) of 17.0@119.3, 14.1@112.8, 12.2@104.4, and 10.8@104.3 for IITR-COF-1 to IITR-COF-4, respectively (Figure 5e), at the current density of 0.12 A g^{-1} . To assess the stability of the electrode material of IITR-COF-1, a self-discharge test was carried out in a $0.5 \text{ M K}_2\text{SO}_4$ (aq) electrolyte. The procedure involved charging the cell up to 2.0 V at a current density of 0.2 A g^{-1} , followed by recording the GCD curve. Subsequently, the cell was allowed to self-discharge (Figure 5f). This curve showed that the voltage decreased to 50% of its peak value within a span of 120 min. Subsequently, it experienced a slow decline and eventually stabilized at a plateau voltage of 0.24 V after 24 h, suggesting a fairly high level of stability.

The cyclic stability of the as-designed SSC of IITR-COF-1 was evaluated through 10,000 cycles at 1.2 A g^{-1} (Figure 5g). The findings reveal excellent stability as the cell maintained 111.3% of its initial capacitance and exhibited a Coulombic efficiency of 97.5%. To assess the capacitive behavior and variations in internal resistance of the designed symmetric cell, EIS measurements were conducted both before and after 10,000 charge–discharge cycles (Figure 5h). The measurements clearly indicate that at higher frequencies, there is an increase in R_s , changing from 0.64 to 6.88Ω . This suggests a slight alteration in the internal resistance of the material, possibly attributed to an increase in the electrode–electrolyte contact during cycles. Besides, at lower frequencies, the plot becomes more vertical after cycling, indicating improved capacitive behavior. A comparison table of the electrochemical performance of IITR-COFs with the recently reported COFs is provided in Table S2. To assess the impact of 10,000 charge–discharge cycles on the functional group, crystallinity, and morphology of the IITR-COF-1 electrode, we conducted FT-IR, PXRD, FE-SEM, and TEM measurements before and after subjecting the electrode to 10,000 GCD cycles. The FT-IR spectra (Figure S7a) revealed that the functional group remained unchanged following the GCD cycles. Notably, peaks corresponding to the imine bond at 1605 cm^{-1} and the (C=N) of the triazene ring at 1506 cm^{-1} were unaffected by the cycle study. PXRD analysis (Figure S7b,c) demonstrated that IITR-COF-1 maintained its crystalline structure after the GCD cycles, underscoring the electrode material's remarkable stability. FE-SEM images (Figure S8) of IITR-COF-1 before and after the charge–discharge cycles showed that the morphology remained the same but the particle size became smaller. This indicates improved wettability, resulting in enhanced accessibility of the electrode–electrolyte interaction for ions, thereby enhancing the capacitive nature. TEM images (Figure S8) displayed minimal morphological changes, with high-resolution transmission electron microscopy (HR-TEM) confirming the presence of fringes in the electrode material. In Figure S8a',b', some spherical shape particles were observed due to the presence of additives (conductor and binder) mixed with the material during electrode fabrication.

To enhance the voltage output, three IITR-COF-1-based symmetric devices were interconnected in series to form a tandem device. Notably, analysis of the cyclic voltammetry (CV) curves reveals that the cell voltage of this device has increased to 6.0 V proportionately with no loss in current density (Figure S9). The performance of the tandem device was further assessed through GCD measurements. It showed nearly a linear charge–discharge curve with a minimal voltage drop (IR). Regarding the practical demonstration of the supercapacitor cell for its storage capacity, it successfully illuminated one white light-emitting

Table 1. Textural Properties and Gas Sorption Values of IITR-COFs

sample code	SA_{BET} ($m^2 g^{-1}$)	pore size (nm)	pore vol (cc g $^{-1}$)	adsorption of CO_2 cc g $^{-1}$ (wt %) (273 and 298 K)	adsorption of H_2 cc g $^{-1}$ (wt %) (77 K)	Q_{st} (kJ mol $^{-1}$)
IITR-COF-1	2830	3.1	1.7	131.9 (25.9) and 51.3 (10.1)	244 (2.18)	25.6
IITR-COF-2	1274	2.3	0.9	78.5 (15.4) and 34.6 (6.7)	168 (1.50)	23.0
IITR-COF-3	876	2.3	0.8	54.0 (10.6) and 24.2 (4.7)	188 (1.06)	21.8
IITR-COF-4	660	2.3	0.5	39.0 (7.6) and 18.6 (3.6)	67.2 (0.60)	21.4

diode (LED) and one red LED using a single cell (Figure S1–i''). The white LED sustained for approximately 1 min and 5 s (Video 1), while the red LED endured for about 3 min and 15 s (Video 2) after charging 50 s.

3.4. Gas Sorption Studies. High surface area controlled textural properties, an electron-rich skeleton, and the presence of heteroatoms have prompted us to investigate the CO_2 sorption and H_2 storage capacities of the synthesized COFs. The CO_2 adsorption capacity of IITR-COFs has been investigated at temperatures of 298 and 273 K and 1 bar pressure, as shown in Figure S10. The CO_2 sorption isotherm at both temperatures has shown a sharp rise in the low-pressure region and a gradual rise in the high-pressure region, but saturation is not achieved. High CO_2 capture capacities of 131.9 cc g $^{-1}$ (25.9 wt %) and 51.3 cc g $^{-1}$ (10.1 wt %) have been observed at 273 and 298 K. Likewise, similar CO_2 sorption isotherm is observed for other COFs. CO_2 capture capacities are observed in the range of 132–39 cc g $^{-1}$ (25.9–7.6 wt %) and 51.3–3.6 cc g $^{-1}$ (10.1–3.6 wt %) at 273 and 298 K, respectively, and follow the order: IITR-COF-1 > IITR-COF-2 > IITR-COF-3 > IITR-COF-4. The order of the CO_2 capture capacities follows the specific surface area and pore volume trend in all of the synthesized COFs. The isosteric heat of adsorption (Q_{st}) for CO_2 sorption calculated using the Clausius–Clapeyron equation was found in the range of 25.6–21.4 kJ mol $^{-1}$, which indicates that the interaction between CO_2 and the COFs is physical in nature, and regeneration of the adsorbent would not be energy intensive (Figure S12). The hydrogen uptake capacity of IITR-COFs was investigated at 77 K and 1 bar. The H_2 isotherm exhibited a rapid rise at the low-pressure region and a gradual rise at high pressure, yet it did not reach saturation. H_2 storage capacity of 244 cc g $^{-1}$ (2.18 wt %) has been observed at 1 bar for IITR-COF-1, and storage capacities of 168 cc g $^{-1}$ (1.5 wt %), 118 cc g $^{-1}$ (1.06 wt %), and 67.2 cc g $^{-1}$ (0.6 wt %) were observed for IITR-COF-2, IITR-COF-3, and IITR-COF-2, respectively (Figure S11). The textural characteristics and gas sorption properties of the four synthesized COFs are outlined in Table 1, while comparisons of their CO_2 and H_2 adsorption properties with the existing literature are provided in Tables S3 and S4, respectively.

4. CONCLUSIONS

In this study, we have successfully synthesized four COFs via Schiff-base polycondensation reaction utilizing the highly flexible trialdehyde linker with four different amine linkers varying in size, symmetry, planarity, and heteroatom content. Surprisingly, IITR-COF-1 was synthesized within 24 h and exhibited superior crystallinity and remarkable reproducibility compared to other COFs. This could be attributed to the large size and high symmetry of the amine monomer in IITR-COF-1, which leads to the rapid formation of the crystalline framework. This outcome indicated that the synthesis of COF can be influenced not only by tautomerization but also by factors such as the size and symmetry of the monomer. It was found that

IITR-COF-1 has the largest SA_{BET} of 2830 m $^2 g^{-1}$ followed by IITR-COF-2 (1274 m $^2 g^{-1}$), then IITR-COF-3 (876 m $^2 g^{-1}$), and finally IITR-COF-4 (876 m $^2 g^{-1}$). All of the synthesized COFs have been investigated for their potential applications in energy storage and gas sorption applications. In a three-electrode setup, the specific capacitance (F g $^{-1}$) reached its peak value of 182.6 for IITR-COF-1, followed by IITR-COF-2 with 156.5, IITR-COF-3 with 138.0, and the lowest value of 118.5 for IITR-COF-4 at in 0.5 M K_2SO_4 (aq) electrolyte. Additionally, all of the materials exhibited impressive energy density (Wh kg $^{-1}$) @power density (W kg $^{-1}$) in a similar trend such as 101.5@298.3 for COF-1, 86.9@284.2 for COF-2, 76.7@283.4 for COF-3, and 65.8@298.3 for COF-4. The symmetric supercapacitor of IITR-COF-1//IITR-COF-1 demonstrated a notable specific capacitance of 30.5 F g $^{-1}$ and an energy density of 17.0 Wh kg $^{-1}$ at a current density of 0.12 A g $^{-1}$ in 0.5 M K_2SO_4 (aq) electrolyte. At the same time, it showed 111.3% of its initial specific capacitance after 10k charge–discharge cycles. The charge storage in all of the materials is influenced by both EDLCs and pseudocapacitance mechanisms. IITR-COF-1 exhibited superior energy storage capacities, which can be attributed to the increased contribution of EDLCs in the energy storage of IITR-COF-1. Our findings suggest that with the combination of EDLCs and PCs, COF-based SCs have great potential to obtain high energy density while maintaining the high power density. Furthermore, IITR-COF-1 displayed a superior CO_2 capture capacity of 25.90 at 273 K and 10.10 wt % at 298 K at 1 bar pressure. It also demonstrated the high H_2 storage capacity of 2.1 wt % at 77 K and 1 bar. These impressive results were attributed to the material's high surface area, pore size, and pore volume. Our study underscores the importance of considering the monomer's size, symmetry, planarity, and heteroatom content when designing COFs for energy storage and gas sorption to solve environment-related challenges.

■ ASSOCIATED CONTENT

SI Supporting Information

The Supporting Information is available free of charge at <https://pubs.acs.org/doi/10.1021/acsami.4c00126>.

Additional experimental details on DFT geometry optimization of monomers; XPS data, PXRD of IITR-COF-1, FE-SEM images, elemental analysis, EDX pattern, and TGA; CV and GCD in two- and three-electrode setup, possible mechanism of redox reactions, FT-IR, PXRD, TEM, and FE-SEM images of IITR-COF-1 electrodes before and after 10k GCD cycles, tandem device analysis, Videos 1 and 2 of LED illumination, and comparison table of electrochemical performance; CO_2 and H_2 adsorption isotherm, and isosteric heat of adsorption (Q_{st}) for CO_2 and comparison tables of the gas adsorption data, and unit cell parameters of all COFs (PDF)

White LED sustained for approximately 1 min and 5 s after charging 50 s (MP4)

Red LED endured for about 3 min and 15 s after charging 50 s ([MP4](#))

AUTHOR INFORMATION

Corresponding Author

Ravindra Pandey – Department of Chemistry, Indian Institute of Technology Roorkee, Roorkee 247667 Uttarakhand, India; orcid.org/0000-0002-4396-9431; Email: rpandey@cy.iitr.ac.in

Authors

Yogesh Kumar – Department of Chemistry, Indian Institute of Technology Roorkee, Roorkee 247667 Uttarakhand, India

Ikrar Ahmad – Department of Chemistry, Indian Institute of Technology Roorkee, Roorkee 247667 Uttarakhand, India

Anuj Rawat – Department of Chemistry, Indian Institute of Technology Roorkee, Roorkee 247667 Uttarakhand, India

Rakesh K. Pandey – Department of Chemistry, Mahatma Gandhi Central University, Motihari 845401 Bihar, India; orcid.org/0000-0003-4314-0532

Paritosh Mohanty – Department of Chemistry, Indian Institute of Technology Roorkee, Roorkee 247667 Uttarakhand, India; orcid.org/0000-0003-2765-0129

Complete contact information is available at:

<https://pubs.acs.org/10.1021/acsami.4c00126>

Author Contributions

Y.K. and R.P. designed the experiments. Y.K. performed the synthesis and characterization of COF materials. Y.K. and A.R. did the adsorption measurements. Y.K. and I.A. did the supercapacitor measurements. Y.K. and R.P. wrote the manuscript. All authors are involved in the discussion and analysis of the results.

Author Contributions

[§]Y.K. and I.A. contributed equally to the manuscript.

Notes

The authors declare no competing financial interest.

ACKNOWLEDGMENTS

R.P. gratefully acknowledges the Ramanujan Fellowship (SB/S2/RJN-060/2017), Core Research Grant (CRG/2018/001474, Science and Engineering Research Board, Government of India), STARS-IISC-MHRD (STARS/APR2019/CS/310/FS), and IIT Roorkee for the financial support. Y.K. and A.R. acknowledge the support from CSIR, Government of India, for a senior research fellowship.

REFERENCES

- (1) Birol, F. *World Energy Outlook 2022* 2022; pp 1–524.
- (2) Ahmad, T.; Zhang, D. A Critical Review of Comparative Global Historical Energy Consumption and Future Demand: The Story Told so Far. *Energy Rep.* **2020**, *6*, 1973–1991.
- (3) Leung, D. Y. C.; Caramanna, G.; Maroto-Valer, M. M. An Overview of Current Status of Carbon Dioxide Capture and Storage Technologies. *Renewable Sustainable Energy Rev.* **2014**, *39*, 426–443.
- (4) Islam, M. S.; Fisher, C. A. J. Lithium and Sodium Battery Cathode Materials: Computational Insights into Voltage, Diffusion and Nanostructural Properties. *Chem. Soc. Rev.* **2014**, *43*, 185–204.
- (5) Niaz, S.; Manzoor, T.; Pandith, A. H. Hydrogen Storage: Materials, Methods and Perspectives. *Renewable Sustainable Energy Rev.* **2015**, *50*, 457–469.

(6) Abe, J. O.; Popoola, A. P. I.; Ajenifuja, E.; Popoola, O. M. Hydrogen Energy, Economy and Storage: Review and Recommendation. *Int. J. Hydrogen Energy* **2019**, *44*, 15072–15086.

(7) Lackner, K. S. A Guide to CO₂ Sequestration. *Science* **2003**, *300*, 1677–1678.

(8) Rackley, S. Carbon Capture and Storage. *Carbon Capture Storage* **2009**, *325*, 1–392.

(9) Wang, F.; Wu, X.; Yuan, X.; Liu, Z.; Zhang, Y.; Fu, L.; Zhu, Y.; Zhou, Q.; Wu, Y.; Huang, W. Latest Advances in Supercapacitors: From New Electrode Materials to Novel Device Designs. *Chem. Soc. Rev.* **2017**, *46*, 6816–6854.

(10) Wang, Y.; Song, Y.; Xia, Y. Electrochemical Capacitors: Mechanism, Materials, Systems, Characterization and Applications. *Chem. Soc. Rev.* **2016**, *45*, 5925–5950.

(11) Miller, J. R.; Simon, P. Materials Science: Electrochemical Capacitors for Energy Management. *Science* **2008**, *321*, 651–652.

(12) Pandey, R. K.; Chen, L.; Teraji, S.; Nakanishi, H.; Soh, S. Eco-Friendly, Direct Deposition of Metal Nanoparticles on Graphite for Electrochemical Energy Conversion and Storage. *ACS Appl. Mater. Interfaces* **2019**, *11*, 36525–36534.

(13) Ahmad, I.; Kumar, A. Nucleotide(s)-Mediated Simultaneous N, P Co-Doped Reduced Graphene Oxide (N, P-RGO) Porous Nanohybrids as High-Performance Electrode Materials for Designing Sustainable Binder-Free High-Voltage (2.8 V) Aqueous Symmetric Supercapacitors and Electrochemical. *Sustainable Energy Fuels* **2022**, *6*, 4169–4182.

(14) Mohamed, M. G.; Sharma, S. U.; Liu, N. Y.; Mansoure, T. H.; Samy, M. M.; Chaganti, S. V.; Chang, Y. L.; Lee, J. T.; Kuo, S. W. Ultrastable Covalent Triazine Organic Framework Based on Anthracene Moiety as Platform for High-Performance Carbon Dioxide Adsorption and Supercapacitors. *Int. J. Mol. Sci.* **2022**, *23*, No. 3174.

(15) Jena, P. Materials for Hydrogen Storage: Past, Present, and Future. *J. Phys. Chem. Lett.* **2011**, *2*, 206–211.

(16) Nandi, S.; De Luna, P.; Daff, T. D.; Rother, J.; Liu, M.; Buchanan, W.; Hawari, A. I.; Woo, T. K.; Vaidhyanathan, R. A Single-Ligand Ultra-Microporous MOF for Precombustion CO₂ Capture and Hydrogen Purification. *Sci. Adv.* **2015**, *1*, No. e1500421.

(17) Vaidhyanathan, R.; Iremonger, S. S.; Shimizu, G. K. H.; Boyd, P. G.; Alavi, S.; Woo, T. K. Direct Observation and Quantification. *Science* **2010**, *330*, 650–653.

(18) Rawat, A.; Muhammad, R.; Chandra Srivastava, V.; Mohanty, P. Identifying the Point of Attachment in the Hypercrosslinking of Benzene for the Synthesis of a Nanoporous Polymer as a Superior Adsorbent for High-Pressure CO₂ Capture Application. *Macromolecules* **2023**, *56*, 1236–1242.

(19) Idrees, K. B.; Li, Z.; Xie, H.; Kirlikovali, K. O.; Kazem-Rostami, M.; Wang, X.; Wang, X.; Tai, T. Y.; Islamoglu, T.; Stoddart, J. F.; Snurr, R. Q.; Farha, O. K. Separation of Aromatic Hydrocarbons in Porous Materials. *J. Am. Chem. Soc.* **2022**, *144*, 12212–12218.

(20) El-Mahdy, A. F. M.; Kuo, C. H.; Alshehri, A.; Young, C.; Yamauchi, Y.; Kim, J.; Kuo, S. W. Strategic Design of Triphenylamine- and Triphenyltriazine-Based Two-Dimensional Covalent Organic Frameworks for CO₂ Uptake and Energy Storage. *J. Mater. Chem. A* **2018**, *6*, 19532–19541.

(21) Han, X.; Xia, Q.; Huang, J.; Liu, Y.; Tan, C.; Cui, Y. Chiral Covalent Organic Frameworks with High Chemical Stability for Heterogeneous Asymmetric Catalysis. *J. Am. Chem. Soc.* **2017**, *139*, 8693–8697.

(22) Liu, X.; Huang, D.; Lai, C.; Zeng, G.; Qin, L.; Wang, H.; Yi, H.; Li, B.; Liu, S.; Zhang, M.; Deng, R.; Fu, Y.; Li, L.; Xue, W.; Chen, S. Recent Advances in Covalent Organic Frameworks (COFs) as a Smart Sensing Material. *Chem. Soc. Rev.* **2019**, *48*, 5266–5302.

(23) Keller, N.; Bein, T. Optoelectronic Processes in Covalent Organic Frameworks. *Chem. Soc. Rev.* **2021**, *50*, 1813–1845.

(24) Kandambeth, S.; Dey, K.; Banerjee, R. Covalent Organic Frameworks: Chemistry beyond the Structure. *J. Am. Chem. Soc.* **2019**, *141*, 1807–1822.

(25) Lohse, M. S.; Bein, T. Covalent Organic Frameworks: Structures, Synthesis, and Applications. *Adv. Funct. Mater.* **2018**, *28*, No. 1705553.

- (26) Haase, F.; Lotsch, B. V. Solving the COF Trilemma: Towards Crystalline, Stable and Functional Covalent Organic Frameworks. *Chem. Soc. Rev.* **2020**, *49*, 8469–8500.
- (27) Ockwig, N. W.; Keeffe, M. O.; Matzger, A. J.; Yaghi, O. M. Porous, Crystalline, Covalent Organic Frameworks. *Science* **2005**, *310*, 1166–1171.
- (28) Dalapati, S.; Jin, S.; Gao, J.; Xu, Y.; Nagai, A.; Jiang, D. An Azine-Linked Covalent Organic Framework. *J. Am. Chem. Soc.* **2013**, *135*, 17310–17313.
- (29) Zhang, X.; Yao, L.; Liu, S.; Zhang, Q.; Mai, Y.; Hu, N.; Wei, H. High-Performance Lithium Sulfur Batteries Based on Nitrogen-Doped Graphitic Carbon Derived from Covalent Organic Frameworks. *Mater. Today Energy* **2018**, *7*, 141–148.
- (30) Furukawa, H.; Yaghi, O. M. Storage of Hydrogen, Methane, and Carbon Dioxide in Highly Porous Covalent Organic Frameworks for Clean Energy Applications. *J. Am. Chem. Soc.* **2009**, *131*, 8875–8883.
- (31) Deblase, C. R.; Silberstein, K. E.; Truong, T. T.; Abruna, H. D.; Dichtel, W. R. B-Ketoenamine-Linked Covalent Organic Frameworks Capable of Pseudocapacitive Energy Storage. *J. Am. Chem. Soc.* **2013**, *135*, 16821–16824.
- (32) Zhao, X.; Pachfule, P.; Thomas, A. Covalent Organic Frameworks (COFs) for Electrochemical Applications. *Chem. Soc. Rev.* **2021**, *50*, 6871–6913.
- (33) Kushwaha, R.; Haldar, S.; Shekhar, P.; Krishnan, A.; Saha, J.; Hui, P.; Vinod, C. P.; Subramaniam, C.; Vaidhyanathan, R. Exceptional Capacitance Enhancement of a Non-Conducting COF through Potential-Driven Chemical Modulation by Redox Electrolyte. *Adv. Energy Mater.* **2021**, *11*, 1–14.
- (34) Zeng, Y.; Zou, R.; Zhao, Y. Covalent Organic Frameworks for CO₂ Capture. *Adv. Mater.* **2016**, *28*, 2855–2873.
- (35) Deng, Q. W.; Ren, G. Q.; Li, Y. J.; Yang, L.; Zhai, S. L.; Yu, T.; Sun, L.; Deng, W. Q.; Li, A.; Zhou, Y. H. Hydrogen and CO₂ Storage in High Surface Area Covalent Triazine-Based Frameworks. *Mater. Today Energy* **2020**, *18*, No. 100506.
- (36) Zhang, Y.; Lu, G.; Zhao, D.; Huang, X. Recent Advances in the Synthesis and Catalytic Applications of Metal-Organic Framework/Covalent Organic Framework Composites. *Mater. Chem. Front.* **2023**, *7*, 4782–4809.
- (37) Sun, Q.; Aguila, B.; Perman, J.; Earl, L. D.; Abney, C. W.; Cheng, Y.; Wei, H.; Nguyen, N.; Wojtas, L.; Ma, S. Postsynthetically Modified Covalent Organic Frameworks for Efficient and Effective Mercury Removal. *J. Am. Chem. Soc.* **2017**, *139*, 2786–2793.
- (38) Jiang, L.; Tian, Y.; Sun, T.; Zhu, Y.; Ren, H.; Zou, X.; Ma, Y.; Meihaus, K. R.; Long, J. R.; Zhu, G. A Crystalline Polyimide Porous Organic Framework for Selective Adsorption of Acetylene over Ethylene. *J. Am. Chem. Soc.* **2018**, *140*, 15724–15730.
- (39) Mondal, S.; Mohanty, B.; Nurhuda, M.; Dalapati, S.; Jana, R.; Addicoat, M.; Datta, A.; Jena, B. K.; Bhaumik, A. A Thiadiazole-Based Covalent Organic Framework: A Metal-Free Electrocatalyst toward Oxygen Evolution Reaction. *ACS Catal.* **2020**, *10*, 5623–5630.
- (40) Zhang, K.; Kirlikovali, K. O.; Varma, R. S.; Jin, Z.; Jang, H. W.; Farha, O. K.; Shokouhimehr, M. Covalent Organic Frameworks: Emerging Organic Solid Materials for Energy and Electrochemical Applications. *ACS Appl. Mater. Interfaces* **2020**, *12*, 27821–27852.
- (41) Das, A.; Mohit, N.; Thomas, K. R. J. Donor-Acceptor Covalent Organic Frameworks as a Heterogeneous Photoredox Catalyst for Scissoring Alkenes to Carbonyl Constituents. *J. Org. Chem.* **2023**, *88*, 14065–14077.
- (42) Yang, M.; Zhou, Z. Recent Breakthroughs in Supercapacitors Boosted by Nitrogen-Rich Porous Carbon Materials. *Adv. Sci.* **2017**, *4*, No. 1600408.
- (43) Chaudhary, M.; Nayak, A. K.; Muhammad, R.; Pradhan, D.; Mohanty, P. Nitrogen-Enriched Nanoporous Polytriazine for High-Performance Supercapacitor Application. *ACS Sustainable Chem. Eng.* **2018**, *6*, 5895–5902.
- (44) Dhiman, N.; Mohanty, P. A Nitrogen and Phosphorus Enriched Pyridine Bridged Inorganic-Organic Hybrid Material for Supercapacitor Application. *New J. Chem.* **2019**, *43*, 16670–16675.
- (45) Lin, L.; Chowdhury, A. U.; Ma, Y.-Z.; Sacci, R. L.; Katsaras, J.; Hong, K.; Collier, C. P.; Carrillo, J.-M. Y.; Doughty, B. Ion Pairing and Molecular Orientation at Liquid/Liquid Interfaces: Self-Assembly and Function. *J. Phys. Chem. B* **2022**, *126* (11), 2316–2323.
- (46) Yadav, I.; Sharma, J. K.; Sankar, M.; D’Souza, F. Symmetrically Functionalized Copper and Silver Corrole-Bis-Tetracyanobutadiene Push-Pull Conjugates: Efficient Population of Triplet States via Charge Transfer. *Chem. - Eur. J.* **2023**, *29*, No. e202301341.
- (47) Khattak, A. M.; Ghazi, Z. A.; Liang, B.; Khan, N. A.; Iqbal, A.; Li, L.; Tang, Z. A Redox-Active 2D Covalent Organic Framework with Pyridine Moieties Capable of Faradaic Energy Storage. *J. Mater. Chem. A* **2016**, *4*, 16312–16317.
- (48) Bhambri, H.; Khullar, S.; Sakshi; Mandal, S. K. Nitrogen-Rich Covalent Organic Frameworks: A Promising Class of Sensory Materials. *Mater. Adv.* **2022**, *3*, 19–124.
- (49) Sekizkardes, A. K.; Wang, P.; Hoffman, J.; Budhathoki, S.; Hopkinson, D. Amine-Functionalized Porous Organic Polymers for Carbon Dioxide Capture. *Mater. Adv.* **2022**, *3*, 6668–6686.
- (50) Li, Z.; Feng, X.; Zou, Y.; Zhang, Y.; Xia, H.; Liu, X.; Mu, Y. A 2D Azine-Linked Covalent Organic Framework for Gas Storage Applications. *Chem. Commun.* **2014**, *50*, 13825–13828.
- (51) Dhankhar, S. S.; Nagaraja, C. M. Porous Nitrogen-Rich Covalent Organic Framework for Capture and Conversion of CO₂ at Atmospheric Pressure Conditions. *Microporous Mesoporous Mater.* **2020**, *308*, No. 110314.
- (52) Afshari, M.; Dinari, M.; Farrokhpour, H.; Zamora, F. Imine-Linked Covalent Organic Framework with a Naphthalene Moiety as a Sensitive Phosphate Ion Sensing. *ACS Appl. Mater. Interfaces* **2022**, *14*, 22398–22406.
- (53) Xu, L.; Ding, S. Y.; Liu, J.; Sun, J.; Wang, W.; Zheng, Q. Y. Highly Crystalline Covalent Organic Frameworks from Flexible Building Blocks. *Chem. Commun.* **2016**, *52*, 4706–4709.
- (54) Zhang, M.; Chen, J.; Zhang, S.; Zhou, X.; He, L.; Sheridan, M. V.; Yuan, M.; Zhang, M.; Chen, L.; Dai, X.; Ma, F.; Wang, J.; Hu, J.; Wu, G.; Kong, X.; Zhou, R.; Albrecht-Schmitt, T. E.; Chai, Z.; Wang, S. Electron Beam Irradiation as a General Approach for the Rapid Synthesis of Covalent Organic Frameworks under Ambient Conditions. *J. Am. Chem. Soc.* **2020**, *142*, 9169–9174.
- (55) Dutta, T. K.; Patra, A. Post-Synthetic Modification of Covalent Organic Frameworks through in Situ Polymerization of Aniline for Enhanced Capacitive Energy Storage. *Chem. - Asian J.* **2021**, *16*, 158–164.
- (56) Li, Y.; Chen, W.; Hao, W.; Li, Y.; Chen, L. Covalent Organic Frameworks Constructed from Flexible Building Blocks with High Adsorption Capacity for Pollutants. *ACS Appl. Nano Mater.* **2018**, *1*, 4756–4761.
- (57) Halder, A.; Kandambeth, S.; Biswal, B. P.; Kaur, G.; Roy, N. C.; Addicoat, M.; Salunke, J. K.; Banerjee, S.; Vanka, K.; Heine, T.; Verma, S.; Banerjee, R. Decoding the Morphological Diversity in Two Dimensional Crystalline Porous Polymers by Core Planarity Modulation. *Angew. Chem., Int. Ed.* **2016**, *55*, 7806–7810.
- (58) Biswal, B. P.; Chandra, S.; Kandambeth, S.; Lukose, B.; Heine, T.; Banerjee, R. Mechanochemical Synthesis of Chemically Stable Isoreticular Covalent Organic Frameworks. *J. Am. Chem. Soc.* **2013**, *135*, 5328–5331.
- (59) Bourda, L.; Krishnaraj, C.; Van Der Voort, P.; Van Hecke, K. Conquering the Crystallinity Conundrum: Efforts to Increase Quality of Covalent Organic Frameworks. *Mater. Adv.* **2021**, *2*, 2811–2845.
- (60) Zhong, C.; Deng, Y.; Hu, W.; Qiao, J.; Zhang, L.; Zhang, J. A Review of Electrolyte Materials and Compositions for Electrochemical Supercapacitors. *Chem. Soc. Rev.* **2015**, *44*, 7484–7539.
- (61) Miao, L.; Song, Z.; Zhu, D.; Li, L.; Gan, L.; Liu, M. Ionic Liquids for Supercapacitive Energy Storage: A Mini-Review. *Energy Fuels* **2021**, *35*, 8443–8455.
- (62) Zhang, H.; Liu, X.; Li, H.; Hasa, I.; Passerini, S. Challenges and Strategies for High-Energy Aqueous Electrolyte Rechargeable Batteries. *Angew. Chem., Int. Ed.* **2021**, *60*, 598–616.

- (63) Thareja, S.; Kumar, A. High Electrochemical Performance of 2.5 V Aqueous Symmetric Supercapacitor Based on Nitrogen-Doped Reduced Graphene Oxide. *Energy Technol.* **2020**, *8*, No. 1901339.
- (64) El-Mahdy, A. F. M.; Hung, Y. H.; Mansoure, T. H.; Yu, H. H.; Chen, T.; Kuo, S. W. A Hollow Microtubular Triazine- and Benzobisoxazole-Based Covalent Organic Framework Presenting Sponge-Like Shells That Functions as a High-Performance Supercapacitor. *Chem. - Asian J.* **2019**, *14*, 1429–1435.
- (65) Halder, S.; Kushwaha, R.; Maity, R.; Vaidhyanathan, R. Pyridine-Rich Covalent Organic Frameworks as High-Performance Solid-State Supercapacitors. *ACS Mater. Lett.* **2019**, *1*, 490–497.
- (66) Li, L.; Lu, F.; Xue, R.; Ma, B.; Li, Q.; Wu, N.; Liu, H.; Yao, W.; Guo, H.; Yang, W. Ultrastable Triazine-Based Covalent Organic Framework with an Interlayer Hydrogen Bonding for Supercapacitor Applications. *ACS Appl. Mater. Interfaces* **2019**, *11*, 26355–26363.